Dalton Transactions

Accepted Manuscript

This article can be cited before page numbers have been issued, to do this please use: B. Orayech, L. Ortega-San-Martín, I. Urcelay-Olabarria, L. Lezama, T. Rojo, M. arriortua and J. M. Igartua, *Dalton Trans.*, 2016, DOI: 10.1039/C6DT02473D.

ROYAL SOCIETY OF CHEMISTRY

www.rsc.org/dalton

View Article Online
DOI: 10.1039/C6DT02473D
ROYAL SOCIETY OF CHEMISTRY

Journal Name

ARTICLE TYPE

Cite this: DOI: 10.1039/xxxxxxxxxx

Effect of partial substitution of Ni by Mg on the structural, magnetic and spectroscopic properties of the double perovskite Sr_2NiTeO_6†

B. Orayech,*[a,c] L. Ortega-San-Martín,[b] I. Urcelay-Olabarria,[c] L. Lezama,[d,e] T. Rojo,[a] María I. Arriortua,[f] and J. M. Igartua [g]

Received Date
Accepted Date

DOI: 10.1039/xxxxxxxxxx

www.rsc.org/journalname

In this report the structural, magnetic and spectroscopic properties of the freeze-drying synthesized $Sr_2Ni_{1-x}Mg_xTeO_6$ (x = 0.0, 0.1, 0.2, 0.3 and 0.5) oxides are analyzed by means of X-ray (XRPD) and neutron diffraction (NPD), electron paramagnetic resonance, diffuse reflectance and magnetic susceptibility. The XRPD and NPD data analysis using mode-crystallography approach have revealed that at room-temperature (RT), all the compositions are monoclinically distorted with the space group $I2/m$. The high and low temperature analysis have shown that these materials suffer a series of three structural phase transitions. The EPR results have shown that the spectra for all the compositions are centred at $g \approx 2.28$, indicating a slightly distorted octahedral environment of Ni^{2+}, which is in agreement with the crystal structure analysis. The increase of Mg^{2+} content in $Sr_2Ni_{1-x}Mg_xTeO_6$, provoke a decrease of the dipolar interaction effects and thus, the resonance becomes narrower. This resonance does not completely disappear which leads to the idea that long-range magnetic order is not completely established when $x \geq 0.3$. The substitution of the Ni^{2+} (S = 1) ions by Mg^{2+} (S=0) ions, also induces the weakening of the antiferromagnetic interactions, which is reflected in the diminishing of: the absolute value of θ and the Néel temperature T_N. The magnetic structures determination revealed the existence of an antiferromagnetic coupling for x- and z-spin components of the nickel atoms.

1 Introduction

The Sr_2NiTeO_6 oxide has been of great interest in the scientific community since the 40's. The first studies focused on its colour (it's yellowish tonality[1] was of interest for the development of ceramic pigments[2]) and its dielectric properties, in case that it could be used in dielectric capacitors.[3,4] The first structural study was done by P. Köhl and co-workers.[5] According to them, the symmetry of the crystal is $C2/m$ and its cell parameters are: a=7.91 Å, b=7.91 Å, c=7.87 Å and β= 90.2°. More precise parameters were provide by D. Iwanaga *et al.*[6] in a more recent work: a=7.9174(4) Å, b=7.8765(4) Å, c=7.916(1) Å and β = 90.378(1)°. The later work suggested that the NiO_6 and TeO_6 octahedra are rotated, out of phase, around one of the three axes of the primitive perovskite. However, all theoretical and experimental studies done up to now show that the symmetry of the crystal structure resulting from this rotation system corresponds to the tetragonal space group $I4/m$, with cell parameters $a = b \approx \sqrt{2}a_p$, and $c \approx 2a_p$.[7] Based on electron diffraction measurements, it has also been suggested that the structure of Sr_2NiTeO_6 as $I12/m1$ symmetry (non-standard setting).[8]

On the other hand the Sr_2MgTeO_6 was recently reported to have tetragonal structure with the space group $I4/m$. These findings, which updated the previous reports of this phase as being cubic, were based on X-ray diffraction, Raman and Infrared spectroscopic investigations.[9] A more recent work has re-examined the previous X-ray diffraction data and has found that the structure appears like a pseudo-tetragonal phase, but the symmetry which describes it best is monoclinic with the space group $I2/m$,[10] which had already been mentioned before by the authors of this

[a] *CICenergigune, Albert Einstein 48, 01510 Miñano, Alava, Spain; E-mail: borayech@cicenergigune.com, orayech@gmail.com*
[b] *Departamento de Ciencias, Sección Química, Pontificia Universidad Católica del Perú (PUCP), Av. Universitaria 1801, Lima-32, Peru.*
[c] *Departamento de Física de la Materia Condensada, Facultad de Ciencia y Tecnología, Universidad del País Vasco, P.O.Box 644, Bilbao 48080, Spain*
[d] *BCMaterials, Technological Park of Biscay, 48160 Derio, Spain.*
[e] *Departamento de Química Inorgánica, Universidad del País Vasco, Apdo. 644, 48080 Bilbao, Spain.*
[f] *Universidad del País Vasco/Euskal Herriko Unibertsitatea (UPV/EHU). Facultad de Ciencia y Tecnología, Dpto. Mineralogía y Petrología, B. Sarriena s/n, 48940, Leioa (Vizcaya), Spain.*
[g] *Fisika Aplikatua II Saila, Zientzia eta Teknologia Fakultatea, Euskal Herriko Unibertsitatea, P.O.Box 644, Bilbao 48080, Spain.*

† Electronic Supplementary Information (ESI) available: [details of any supplementary information available should be included here]. See DOI: 10.1039/b000000x/

View Article Online
DOI: 10.1039/C6DT02473D

work.[11] This is why the structural analysis of the compositions presented in this paper has been done carefully and paying special attention to previous inconsistencies.

The present paper presents a complete analysis on the $Sr_2Ni_{1-x}Mg_xTeO_6$ perovskite oxides, where the spectroscopic, magnetic and structural data at different temperatures are presented for the first time. The crystal structure of all the oxides has been studied from low to high temperature by X-ray diffraction (in all cases) and neutron diffraction (the latter just with x=0 and x=0.1 compounds and up to room temperature) in order to investigate the sequences of phase transitions and find if these oxides follow the behavior of similar Sr_2BTeO_6 compounds with B=Mn^{2+} and Co^{2+} which crystallize in a more distorted perovskite structure at room temperature compared to the nickel phase.[8,12,13] The existing data on the room temperature structure for the parent compound (x=0)[8] are reviewed using mode-crystallography,[13–16] which is also applied to the other phases for the first time. The impact of substitution of Ni cation by Mg cation on the magnetic and spectroscopic properties of the double perovskite Sr_2NiTeO_6 are evaluated in accordance with the structural results. The magnetic structures of Sr_2NiTeO_6 and $Sr_2Ni_{0.9}Mg_{0.1}TeO_6$ are solved making use of the full symmetry of the materials, as deduced from the diffraction experiments and from the magnetic properties.

2 Experimental

Polycrystalline $Sr_2Ni_{1-x}Mg_xTeO_6$ with x = 0.0, 0.1, 0.2, 0.3 and 0.5 were synthesized by the freeze-drying method. Stoichiometric quantities of $SrCO_3$, $Ni(C_2H_3O_2)_2$, $Mg(C_2H_3O_2)_2$ and TeO_2 were dissolved in dilute aqueous nitric acid. The solutions were drop-by-drop frozen under liquid nitrogen. The frozen solutions were subsequently freeze-dried and the powders obtained were ground and calcined at 1170 K for 6 hours. The samples were ground, pelleted and calcined for 8 hours at 1320K. Phase purity was confirmed by X-ray powder diffraction and the expected content of Sr, Ni, Mg and Te in $Sr_2Ni_{1-x}Mg_xTeO_6$ was verified by inductively coupled plasma atomic emission spectroscopy (ICP-AES) performed with an ARL Fisons 3410 spectrometer (see Table **??**) **(ESI†)**.

Spectroscopic measurements were made by both Diffuse Reflectance and Electron Paramagnetic Resonance (EPR). The diffuse reflectance spectrum was collected on a Cary 2415 spectrometer and registered at RT in the 5000-50000 cm^{-1} range. X-Band EPR spectra were recorded between 0 and 7 kOe from 300 to 5 K on a Bruker ESP 300 spectrometer. The temperature was controlled by an Oxford Instruments (ITC4) regulator. The magnetic field was measured with a Bruker BNM 200 gauss-meter and the frequency inside the cavity was determined using a Hewlett-Packard 5352B microwave frequency counter.

DC magnetic susceptibility measurements were performed using a Quantum Design MPMS-7 SQUID magnetometer whilst heating from 5 to 300 K in an applied field of 1 kOe for composition x = 0.0, 0.1, 0.2 and 0.3, after cooling either in the absence (zero-field cooling, ZFC) or presence (field cooling, FC) of the applied field.

Magnetization as a function of applied field H was measured using the same MPMS-7 SQUID magnetometer at 5 K after cooling the sample in zero field. During the measurement, the field was swept between 70 and 270 kOe.

Neutron powder diffraction (NPD) experiments were carried out at the Institut Laue Langevin (ILL), Grenoble, France, on D2B high-resolution diffractometer. For the experiment, polycrystalline samples of Sr_2NiTeO_6 and $Sr_2Ni_{0.9}Mg_{0.1}TeO_6$ were packed in an 8 mm diameter vanadium can, which was held inside a liquid helium cryostat. Data were collected at 4, 60 and 298 K in the Sr_2NiTeO_6 composition and at 4 and 298 K on $Sr_2Ni_{0.9}Mg_{0.1}TeO_6$; using the wavelength $\lambda = 1.595$ Å in the angular range $2^\circ \leq 2\theta \leq 162^\circ$ in steps of 0.05° with an integration time of 50000 monitor counts per step. Each point in the diffraction pattern was recorded by 6 independent detectors for subsequent normalization and summation, giving an overall collection time of approximately 3 hours for the entire data set.

Temperature dependent neutron powder diffraction data were collected on Instrument D1B at the ILL. Neutrons of wavelength 2.52Å were used. Data were collected every 1.5 K from 2 to 37 K over the angular range $10^\circ \leq 2\theta \leq 90^\circ$. Sequential refinement was carried out in FullProf.

Room-temperature X-ray powder diffraction (XRPD) data were collected in the range $18 \leq 2\theta \leq 102^\circ$ in steps of 0.02° with an integration time of about 15 seconds per step using a Philips X'Pert MPD X-ray diffractometer with secondary beam graphite monochromatizated Cu-Kα radiation. The room-temperature crystal-structure was refined simultaneously from X-ray and high-resolution neutron diffraction data. Temperature resolved XRPD data were collected using an Anton Pår HTK16 temperature chamber with a platinum stage mounted in the same diffractometer. The sample for high temperature measurement was mixed with acetone and a high temperature resin and applied to the Pt stage. To monitor the evolution of several characteristic peaks, data were collected every 10 K from 320 to 820 K in the angular ranges $74.6^\circ \leq 2\theta \leq 77.2^\circ$, $83.2^\circ \leq 2\theta \leq 85.5^\circ$ and $92.0^\circ \leq 2\theta \leq 95^\circ$. Higher quality, temperature-dependent XRPD data for subsequent Rietveld refinement were collected in the range $17^\circ \leq 2\theta \leq 87^\circ$ in steps of 0.02° with an integration time of 12 seconds per step, between 300 and 770 K, every 50 K.

Diffraction data were treated using the FullProf Suite program package[17] and Jana2006.[18] Magnetic structures were plotted using Vesta program.[19]

3 Results and Discussion

3.1 Spectroscopic measurements

3.1.1 Diffuse reflectance

Figure 1 shows the spectra measured in the (3000-35000) cm^{-1} energy interval obtained for the compositions $Sr_2Ni_{1-x}Mg_xTeO_6$ with x = 0.0, 0.1, 0.2, 0.3 and 0.5. In all cases, five bands show up, being three of them very intense and the other two much weaker. The band assignment has been done based on the Tanabe-Sugano energy diagrams for a d^8 metal such as Ni^{2+} ion.[20] The most intense bands correspond to the spin allowed transitions between the fundamental state $^3A_{2g}(^3F)$ and the excited states $^3T_{2g}(^3F)$, $^3T_{1g}(^3F)$ and $^3T_{1g}(^3P)$. The less intense

View Article Online
DOI: 10.1039/C6DT02473D

bands emerge due to prohibited spin transitions that, given their position, correspond to electronic excitations from the fundamental state $^3A_{2g}(^3F)$ to the $^1E_g(^1D)$ and $^1T_{2g}(^3D)$ states. Table 1 gathers the values of the energies of the bands of each composition, together with the *Dq* and *B* parameters. Note that the Racah parameter B is 80 % of the value of the free ion, B_{free}, in good agreement to the usually observed values ($0.7B_{free} < B < 0.9B_{free}$).[21]

3.1.2 EPR spectroscopy

In principle, no spin-orbit coupling is expected for a Ni^{2+}, d^8, cation due to the different symmetry between the fundamental state ($^3A_2$ singlet) and the high-energy terms (^3T triplets). However, the wave functions of the fundamental state are slightly affected by the ^3T terms in such way that the former is modified by a second order spin-orbit coupling. Moreover, the $^3A_2$ can be splitted by the presence of an external field.[22,23] The degeneracy of those energy levels can be studied by EPR spectroscopy by observing the deviation of the experimental *g* tensor with respect to the value of the free ion. In general, the tensor is isotropic with values between 2.15 and 2.35. In an ideal octahedron, where the effects of covalent bonds are not taken into account, the g value can be approximated using the diffuse reflectance data calculated before using the equation:

$$g = 2.0023(1 - \frac{4\lambda_{so}}{10Dq}) \quad (1)$$

where λ_{so} is the second order spin orbit constant (= -300cm^{-1}). Using the data from Table 1, we obtain an approximate value of g= 2.35 in all cases.

The normalized EPR spectra collected at RT for all the crystals are plotted in Figure 2a. The observed signals are wide, isotropic and they are centered at $g \approx 2.28$ which is very similar to that obtained from diffuse reflectance. These values are characteristic for a slightly distorted octahedral environment of Ni^{2+}.

The curves have been fitted, see Figure 2b, using the derivative of the Lorentz function, from which the *g* tensor and the peak to peak linewidth (ΔH_{pp}) have been taken. Even if the value of the *g* tensor is equal for all the compositions, 2.28, ΔH_{pp} decreases as the amount of Ni decreases, see Figure 2c. This behavior is consistent with the dilution effect of Ni^{2+} ions in the structure whilst it is substituted by Mg^{2+}. The resulting increase of the distance between the nickel ions decreases the dipolar interaction effects and thus, the resonance becomes narrower.

Figure 3a shows the temperature dependence of the spectra on cooling for x = 0.0, 0.3 and 0.5 compositions. The values of the integrated area of the signal (A_{EPR}, that is usually considered as the EPR susceptibility) and the peak to peak amplitude, ΔH_{pp}, are shown in Figure 3b.

The A_{EPR} parameter exhibits the same tendency in all compositions: as the temperature decreases, it smoothly increases its value up to a maximum, and with further decreasing temperature it falls down abruptly. In contrast, the resonance line-width has the opposite behavior: it decreases gradually with the temperature down to a minimum, below which it grows considerably fast, see Figure 3. Such evolution of the A_{EPR} is typical in systems with weak magnetic interactions: the number of spins capable to resonate under field increases with decreasing temperature, until the system reaches the temperature at which the strong magnetic correlations arise between the spins of Ni^{2+} ions and, thereafter, the A_{EPR} decreases rapidly. The relaxation time of the spins is related to the evolution of the ΔH_{pp} parameter. As the temperature falls down, the relaxation time of the spins is reduced and, in consequence, the resonance line-widths become narrower. Below certain temperature, the exchange interactions and the dipolar effects considerably increase, and the line-widths start broadening. This effect is better observed in the substituted compositions because, as the amount of the Ni^{2+} cations decreases in the composition, the interactions between Ni^{2+} cations become more difficult and, thus, the broadening of the curves takes place at lower temperatures.

At sufficiently low temperatures, in the magnetically ordered state, the resonance almost disappears, see inset Figure 3a, x=0 sample. In the pure Sr_2NiTeO_6 composition this effect occurs at 18 K. As the amount of Mg increases, the resonance does not completely disappear which leads to the idea that long-range magnetic order is not completely established when $x \geq 0.3$.

3.2 Magnetic properties

In the paramagnetic region, the evolution of the inverse of the magnetic susceptibility as a function of the temperature exhibits the behavior described by the Curie-Weiss law, see Figure 4, and therefore all the curves have been fitted accordingly. The resulting C_m and θ parameters are gathered in Table 2. The negative values of the Weiss temperature and the descending tendency of the magnetic susceptibility below the critical temperature indicate the antiferromagnetic character of the materials.

The substitution of the Ni^{2+} ions by Mg^{2+} ions induces the weakening of the antiferromagnetic interactions, which is reflected in the diminishing of the absolute value of θ and the Néel temperature T_N, see Table 2. In any case, the effective magnetic moment values obtained from the fittings are in good agreement with the expected values for a Ni^{2+} ion in high-spin state.

The $\frac{J_1}{J_2}$ ratio shown in Table 2 has been calculated considering the work of G. Blasse[24] on the magnetic behavior of perovskites. He proposed that the θ and T_N parameters were directly related to the exchange-coupling constants between the next neighbors (NN, located at 90° from each other), given by J_1, and between next-nearest neighbors (NNN, located at 180°), reflected by J_2 (see Figure 5a). The relation between those constants has often been used to predict the magnetic order in double perovskites which, in the case that only one B cation is paramagnetic, are divided in two main types: type I (Figure 5b) and type II (Figure 5c).[25–27] The values shown in Table 2 suggest that the magnetic ordering in all the compositions is a Type I antiferromagnetic spin-arrangement, which consists of layers of ferromagnetic configuration antiferromagnetically coupled. In this arrangement there is some degree of frustration because 8 of the 12 NN nickel ions are antiferromagnetically coupled and 4 are ferromagnetically coupled.

From the evolution of the magnetic susceptibility, χ_m, as the

View Article Online
DOI: 10.1039/C6DT02473D

temperature decreases, it is possible to observe that the increase of Mg gives rise to a paramagnetic contribution at low temperatures, revealed by small tails at temperatures below T_N. At $x = 0.3$ the amount of Mg is high enough that the maximum of the susceptibility is difficult to observe, hindering the determination of the Néel temperature. This is probably the result of the simultaneous interruption of the magnetic interactions resulting from the presence of the diamagnetic Mg^{2+} ion instead of the paramagnetic Ni^{2+} ions and also from the presence of some antisite disorder in the Ni/Mg and Te positions in the substituted phases, as indicated in Table 3. This antisite disorder contributes to the frustration in the antiferromagnetic interactions and enhances the paramagnetic contribution at low temperature.

In any case, the high intensity of the antiferromangnetic coupling is confirmed by the zero-field-cooled (ZFC) and field-cooled (FC) susceptibility measurements, plotted in Figure 6, where no irreversibility is observed. This result disagree with those presented by Iwanaga et al. in[6] who observed a big irreversibility in the ZFC and FC curves. This discrepancy is attributed to the experimental process: they measured ZFC and FC curves using 100 Oe and 30 kOe fields. In contrast, in the present work, the same field (1 kOe) was used for both measurements, which leads to the conclusion that the process is completely reversible. In fact, the magnetization in the pure Sr_2NiTeO_6 composition measured at 5 K after cooling under 100 Oe field showed no hysteresis as expected for this system. (see Figure **??**) **(ESI†)**.

3.3 Crystal Structures: High Temperatures and Room Temperature

Room temperature X-ray and neutron powder diffraction data in all cases were indexed in the same space group as the parent compounds (x=0 and x=1): the $I2/m$ space group. It is to note that the Rietveld refinements to these data have been carried out using mode crystallography. In the case of the RT monoclinic space group $I2/m$, there are four irreducible representations (irreps) of the $Fm\bar{3}m$ space group, that can take part in the symmetry breaking, and these are, as shown in Table 2 in ref.[14]: $GM_1^+(1)$ (totally symmetric), $GM_3^+(1)$, $GM_4^+(1)$ and $GM_5^+(4)$. Previous studies using the same approach,[11,13,14,16,28] have shown that the system does not use all the symmetry modes available (some displacements with respect to the prototype phase are permitted but they are not found experimentally). Consequently, from all the mode amplitudes that are available for the $I2/m$ space group to describe the room temperature distortion from the ideal perovskite, only GM_4^+ (the one that describes the tilting of the BO_6 octahedra) has been used. Rietveld fits to the RT data are shown in Figure 7. Results from the fits are in Tables 3 and 4. Figure 8 shows the results of the mode amplitude and cell parameters at RT for all phases. The values for the amplitudes are very similar, although they show a very slight decrease with x, which indicates that the monoclinic distortion at room temperature is not substantially affected by the magnesium doping.The cell parameters show a slightly changing trend, with a small reduction of the volume with increasing x. This effect is consistent with the increase of GM_4^+ with decreasing x and also with the increase of the tolerance parameter as x approaches 0.

Low temperature neutron diffraction on x=0 phase (Sr_2NiTeO_6) showed the presence of several new peaks that did not appear at room temperature (Figure 9a). Given that the onset of magnetic ordering occurs below 35K, only the new peaks that appear in the 60K data set are of structural origin. These new reflections were indexed considering the typical $P2_1/n$ space group for monoclinically distorted double perovskites. This new low temperature structure indicates that a structural transition exist between RT and 60K. This transition is the same observed above room temperature in Sr_2BTeO_6 family (B= Co, Mn).[11,13,14,29] The data at 4K, below the magnetic transition temperature, show the presence of new peaks that belong to the magnetic ordering, which will be discussed later.

The $I2/m \rightarrow P2_1/n$ transition also occurs in the x=0.1 phase (Figure 9b). In the light that the same sequence of phase transitions that occur in the Co and Mn phases would repeat in these compounds several important peaks of the RT XRD patterns were studied by thermodiffractometry (Figure 10). The changes observed for the x=0 phase are consistent with the changes previously observed in the Mn and Co phases, confirming the same sequence of phase transitions: $Fm\bar{3}m \rightarrow I4/m \rightarrow I2/m \rightarrow P2_1/n$. The group of reflections that appear in the $74.6^\circ \leq 2\theta \leq 77.2^\circ$ range (which show changes in each transition) was also studied in all the substituted phases (see Figure **??**) **(ESI†)** and it confirmed that the same sequence of transitions occurs in this case.

The evolution of the structure with temperature has been studied, again, by mode crystallography. The mode-amplitudes describing the distorted phases that we have followed from the more distorted phase ($P2_1/n$) at low temperatures are GM_4^+ (the one that describes the tilting of the BO_6 octahedra), X_3^+ (the primary order parameters) and X_5^+ ,trillinearly coupled to the formers, and always necessary for the convergence of the refinement. In the other two intermediate phases $I2/m$ and $I4/m$ only GM_4^+ was present. The values for those amplitudes obtained from the NPD data, assuming to be the best possible values, have been the ones used for the refinements of the XRPD data. We have also refined the XRPD data assuming we did not have the NPD data and the obtained amplitude-values are very close but with bigger error bars. The GM_4^+ irrep is the same in both intermediate phases but it is not oriented in the same way, as indicated in previous works.[30] This is the only mode-amplitude refined freely in the $I2/m$ and $I4/m$ phases. This means that the distortion present in these phases consists only on the tilting of the octahedra. There is another distortion not described by the mentioned mode (GM_4^+ irrep): the deformation of the cell. In a first approximation, we can analyse these two distortions separately, considering them as independent.[31]

In summary: GM_4^+ irrep consists in a tilting around the tetragonal axis that starts (and then evolves in a continuous way) when the cell transforms and the structure passes from cubic to tetragonal. The GM_4^+ distortion continues until the cell does not stand more tilt-distortion and changes to a monoclinic system.

We have observed that the sole freed amplitude in the monoclinic phase does not change, in the first refinement, in which we have freed the atomic displacements parameters, see Figure 11a.

View Article Online
DOI: 10.1039/C6DT02473D

Usually, we do free the atomic displacements parameters in the final stages of the refinements and, usually, with some restrictions. The atomic displacement parameters (ADP) have been refined with restrictions and only three ADP have been considered: Sr position, B-site atoms (which have been coupled together and also oxygen atoms (also coupled even if there were more than one position). In this way a stable refinement is achieved but the structural freedom is maintained. The high temperature study of $SrZrO_3$ and $CaTiO_3$ with neutron diffraction carried out by Kennedy et al.,[32], has demonstrated that ADPs at high temperature are highly anisotropic. Laboratory high temperature XRPD data is not suitable for this detailed refinement so isotropic ADP have been used. As a first approximation we used their B_{iso} in the high temperature refinements.

A nearly pseudo-linear behavior has been observed, as can be seen in Figure 11b (red curve). The slope for the oxygen B_{iso} is approximately twice that of the rest of the atoms, which is quite reasonable; taking into account the other atoms present. With this two slopes, we have calculated the fitted values for the B_{iso} at each experimental temperature. We have refined again all the data freeing everything, as previously described, except the B_{iso}: fixed by the fitted values. The results are shown in Figure 11b (blue curve). For comparison, the black curve is also shown in Figure 11b.

In the tetragonal phase, the amplitude values show a diminishing trend, as expected in the case of a second order phase transition. They go to zero with a nearly square root dependence with the temperature. This is the fitting result to a Landau Theory second order phase transition with a continuous behavior of the primary order parameter: and with increasing errors, which also agrees with the expected behavior for those kind of phase transitions, as the fluctuations, in a mean field theory, increase as the distance to the phase transitions diminishes. On the other hand, in the case of the monoclinic intermediate phase, the distortion does not show a so big diminishing trend: it maintains almost constant. The errors corresponding to this mode-amplitude values are smaller and more homogeneous. Finally, there is a jump between the values of the distortion mode-amplitude: even if both modes represent the same collective displacement pattern, they are oriented in different directions, referred to the prototype cubic, so the phase transitions has a strong first order character, as it is clearly seen in the obtained results. Subsequent combinations of B_{iso} sets have not changed the described picture.

Results from the high temperature fits are shown in Figure 11 and 12. The observed behavior indicates that, as the temperature is lowered, the cell contracts but the tilts increase. The release of the energy on cooling is different in each variable: the oxygen displacement (represented by the tilts) change smoothly even during some structural transitions, but the cell parameters vary smoothly only while the structure is the same and abruptly in the transition. When the compounds transform to the lowest symmetry structure, new mode-amplitudes appear but they remain reasonably constant with the exception of the GM_4^+, which indicate that the tilts are the most important distortion in operation.

3.4 Low-Temperature magnetic structures

As it was indicated before (see Figure 9) 4K neutron powder diffraction data showed the presence of extra reflections of magnetic origin. Those new reflections correspond to the magnetic ordering and can be indexed by $\mathbf{k} = (0, 0, 0)$ propagation vector. The crystal structure does not undergo any additional distortion induced by the magnetic transition.

The symmetry analysis done to figure out the possible magnetic symmetries compatible with the data is explained in detail in reference[13]. Just a note to recall that the full symmetry of the parent group is in this case $P2_1/n1'$ and the magnetic ordering should be described by a subgroup of the parent group (paramagnetic), where the time-reversal operation is not present. The maximal subgroups of the parent group compatible with $\mathbf{k} = (0, 0, 0)$ and which allow magnetic ordering for Ni atoms located in $(0\,0\,\frac{1}{2})$ position are $P2_1/n$ and $P2_1'/n'$. These magnetic groups are the outcome of the activation of the magnetic irreps $mG1+$ and $mG2+$ of $P2_1/n1'$, respectively.

Neutron diffraction data at 4 K of both compositions have been analyzed using $P2_1/n$ and $P2_1'/n'$ magnetic space groups. The magnetic structures of both compositions have $P2_1/n$ symmetry. The fittings are shown in Figure 13 and the resulting crystal-structures are given in Table 5. It is clearly observed that the refinement with the $P2_1'/n'$ space group does not fit well the magnetic reflections, whereas $P2_1/n$ symmetry does. The magnetic components obtained from the refinements are given in Table 6. Within experimental error, there is no difference between the magnetic structure of the pure Sr_2NiTeO_6 and that of $Sr_2Ni_{0.9}Mg_{0.1}TeO_6$. The spin arrangement consists of ferromagnetic layers antiferromagnetically coupled along the c axis, as it was already predicted from the J_1/J_2 ratio calculated from the magnetic susceptibility data. In each layer the spins are parallel within the ac plane, making an angle δ with the c axis: $\delta = 42(3)^\circ$ and $\delta = 43(3)^\circ$ for the $x = 0.0$ and $x = 0.1$ compositions, respectively. However, the refinements are not conclusive in the sense that they are indistinguishable for δ and $-\delta$ values, see Figure 14, and consequently none of these results can be disregarded.

It is to note, however, that the magnetic moment observed at low temperature (1.8 μ_B) is smaller than the effective paramagnetic moment obtained in the paramagnetic region (2.9–3.9 μ_B). Even if the low temperature magnetic moment is approximated as $M = gS$, where g is the gyromagnetic factor determined from EPR and S the total spin quantum number (S=1 for a d^8 ion), the observed magnetic moment at 4K is smaller than the calculated from the previous formula (2,28 μ_B). This is common in all double perovskites containing Ni as the sole paramagnetic ion (Table 7). This could be attributed to the type of antiferromagnetic orderings observed in these perovskites and the frustration that is inherent to such configurations: in the present type I case of the 12 NN atoms around a given nickel ion 8 are coupled antiferromagnetically (at a distance of 5.58Å) whereas the 4 remaining NN Ni ions in the ab plane (two of which are at 5.56 Å and another two are separated 5.60 Å) are coupled ferromagnetically. This was already observed in the $Sr_2Co_{1-x}Mg_xTeO_6$ system, with also a type I antiferromagnetic ordering, which showed a greater

View Article Online
DOI: 10.1039/C6DT02473D

reduction of the magnetic moment compared to the expected paramagnetic one.[13] Similar compounds such as Sr_2CuWO_6[33] or $BaLaCuSbO_6$[34] do not even show a three-dimensional antiferromagnetic ordering at low temperature. Although the Ni phases differ from the latter because in a Ni (II) ion both $d_{x^2-y^2}$ and d_{z^2} orbitals are available for a three-dimensional magnetic ordering, whereas in the Cu(II) phases only a two-dimensional magnetic ordering is possible, the frustration present might be responsible for a reduction of the intensity of the interactions and, thus, of the observed magnetic moment. The broad magnetic peaks observed in the magnetic susceptibility measurements in the present case, which resemble those of the copper phases -but to a lesser extent-, would be in favor of this interpretation.

Supplementary Figure **?? (ESI†)** shows the temperature dependent D1B diffraction data. The thermal dependence of the magnitude of the magnetic moment is represented as inset. It can be observed that the three-dimensional magnetic order begins on cooling below 35K, as expected from magnetic susceptibility and EPR data.

4 Conclusions

The double perovskites $Sr_2Ni_{1-x}Mg_xTeO_6$ (with x = 0.0, 0.1, 0.2, 0.3 and 0.5) have been successfully synthesized by the freeze-drying method. The room-temperature crystal-structures of all the compositions are monoclinic with space group symmetry $I2/m$. The structures reported in the present work, have been described and refined in the framework of mode-crystallography approach. $Sr_2Ni_{1-x}Mg_xTeO_6$ undergoes three structural phase transitions with increasing temperature, with the sequence: $P2_1/n \rightarrow I2/m \rightarrow I4/m \rightarrow Fm\bar{3}m$. As in the case of the $Sr_2Co_{1-x}Mg_xTeO_6$ system, only three relevant modes GM_4^+, X_3^+ and X_5^+ in $P2_1/n$, and only one, GM_4^+, in $I2/m$ and $I4/m$ have been shown to contribute to the distorted structures observed experimentally. The GM_4^+ irrep is the same in both intermediate phases, $I2/m$ and $I4/m$, although it is not oriented in the same way. The amplitudes of the distortion produced by the GM_4^+, goes to negligible value at a second order transition. A parameterized combinations of B_{iso} have been set to get the good diminishing trend of the amplitudes with the temperature increase. Replacing the ion Ni^{2+} by Mg^{2+}, hardly changes the distortion.

The five bands that show up in the diffuse reflectance measurements correspond to the spin transitions between the fundamental state $^3A_{2g}(^3F)$ and the excited states $^3T_{2g}(^3F)$, $^3T_{1g}(^3F)$,$^3T_{1g}(^3P)$, $^1E_g(^1D)$ and $^1T_{2g}(^3D)$. The obtained Dq and B parameters are in good agreement to the usually observed values ($0.7B_{free} < B < 0.9B_{free}$).

The EPR results have shown that the spectra for all the compositions are centred at $g \approx 2.28$, which are similar to the calculated values from diffuse reflectance data considering a second order spin-orbit coupling. These values are characteristic for a slightly distorted octahedral environment of Ni^{2+}, in agrement with the data obtained from the crystal structure analysis. It has been shown that the increase of the distance between the nickel ions decreases the dipolar interaction effects and thus, the resonance becomes narrower. At low temperatures, EPR data of the Sr_2NiTeO_6, confirm the change in the magnetic properties of nickel, where the resonance almost disappears around 35K. As the doping with Mg increases, the resonance does not completely disappear indicating that long-range magnetic order is not completely established when $x \geq 0.3$.

Strong antiferromagnetic interactions between nickel ions (evidenced by the reversibility of ZFC/FC curves and the high θ) were observed which are progressively weakened by the substitution of the Ni^{2+} (S = 1) ions by Mg^{2+} (S=0), as evidenced by the reduction of the Néel temperature with x. The magnetic structures of Sr_2NiTeO_6 and $Sr_2Ni_{0.9}Mg_{0.1}TeO_6$ have been solved and they can be described using the same space group as the crystal structure at low temperature, $P2_1/n$. This imposes an antiferromagnetic coupling for x- and z-spin components and a ferromagnetic coupling for the y-spin component between the Nickel atoms.

The magnetic moments at low temperature are smaller than expected and this has been attributed to the frustration resulting from this antiferromagnetic ordering.

Acknowledgments

We are grateful for financial support from the Basque Government (IT-282-07 and IT-779-13), the Ministry of Economy and Competitiveness (MINECO)(MAT2012-34740) and the University of the Basque Country under the fellowship 'Especialización de Personal Investigador del Vicerrectorado de Investigación de la UPV/EHU'. Thanks for Aitor Larrañaga from SGIker (UPV/EHU) general services for the XRPD measurements.

View Article Online
DOI: 10.1039/C6DT02473D

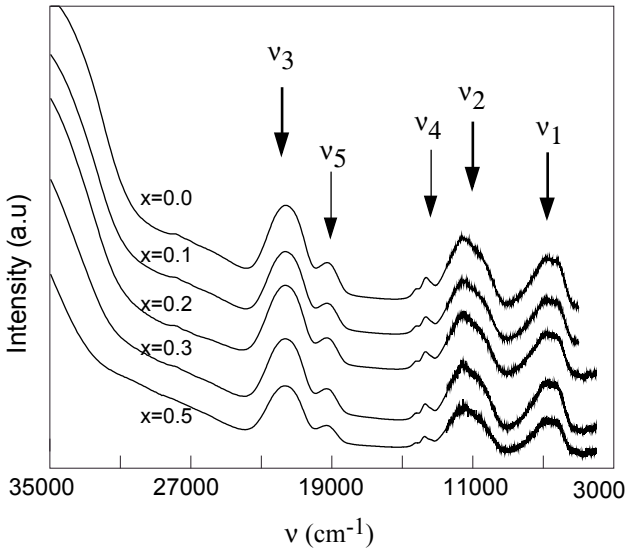

Fig. 1 Diffuse reflectance spectra of the $Sr_2Ni_{1-x}Mg_xTeO_6$ (x=0.0, 0.1, 0.2, 0.3 and 0.5) series, in the energy range of 3000-35000 cm^{-1}.

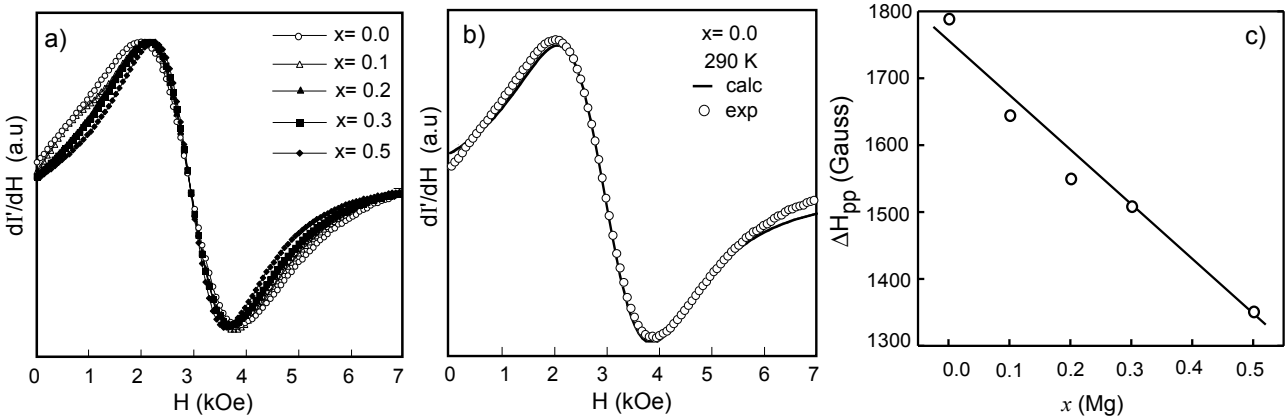

Fig. 2 a) Normalized EPR spectra at RT of the $Sr_2Ni_{1-x}Mg_xTeO_6$ (x = 0.0, 0.1, 0.2, 0.3 and 0.5) series. b) Fitting of the x = 0.0 curve using the derivative of a Lorentzian function. c) Resonance line-widths (ΔH_{pp}) of the $Sr_2Ni_{1-x}Mg_xTeO_6$ (x = 0.0, 0.1, 0.2, 0.3 and 0.5) series at RT.

View Article Online
DOI: 10.1039/C6DT02473D

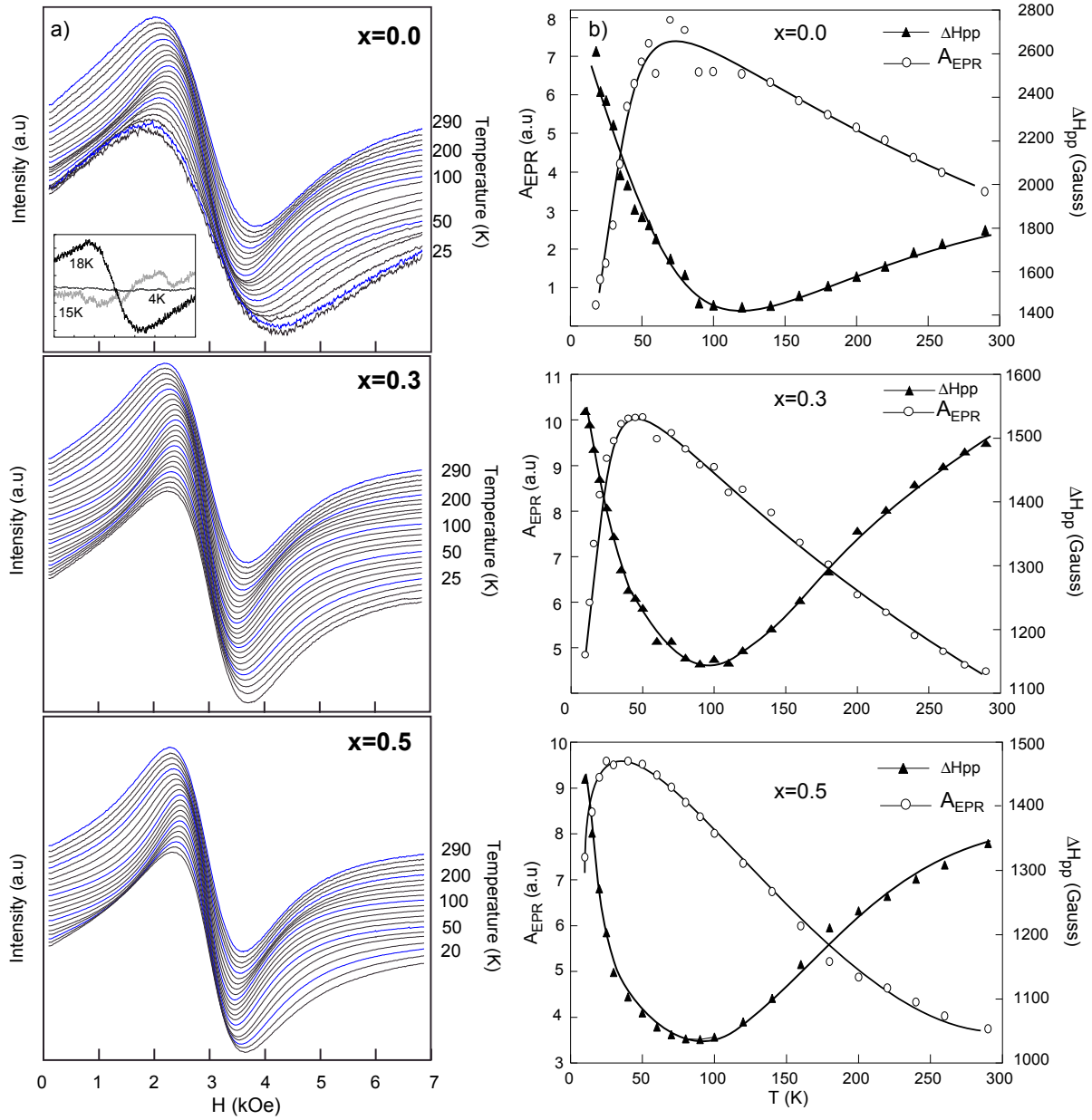

Fig. 3 a) EPR spectra collected at different temperatures for ($x = 0.0, 0.3$ and 0.5) of the $Sr_2Ni_{1-x}Mg_xTeO_6$ series. b) Thermal evolution of the peak to peak line widths (ΔH_{pp}) and the integrated area of the EPR signals for ($x = 0.0, 0.3$ and 0.5), in the $Sr_2Ni_{1-x}Mg_xTeO_6$ series. Solid lines shown in the figure 3b are just guides for the eye.

View Article Online
DOI: 10.1039/C6DT02473D

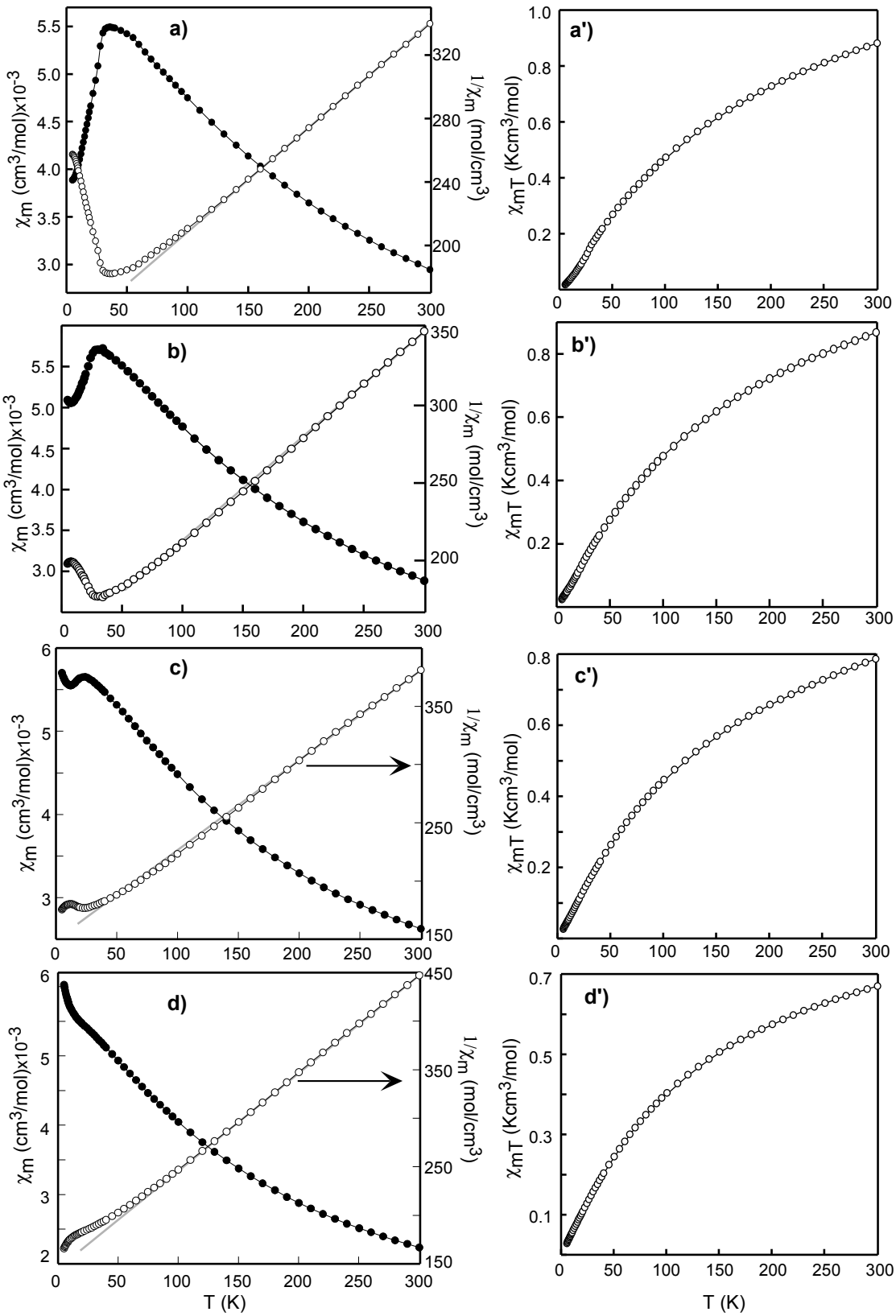

Fig. 4 (a-d) Susceptibility and its inverse curves for the (x = 0.0, 0.1, 0.2 and 0.3) series. In grey, the fitting according to the Curie-Weiss law is shown.

View Article Online
DOI: 10.1039/C6DT02473D

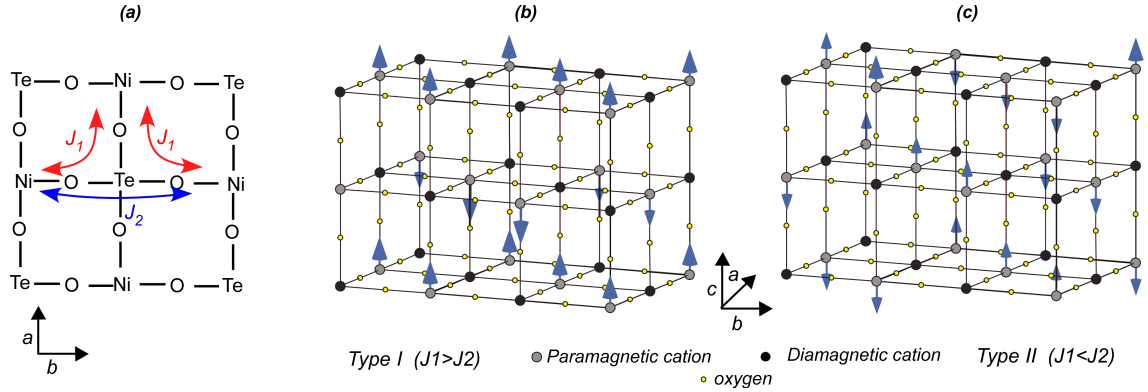

Fig. 5 The two types of exchange couplings expected in the double perovskite (a) and schematic representation of the two main magnetic structure types usually observed in these perovskites, type I (b) and type II (c).

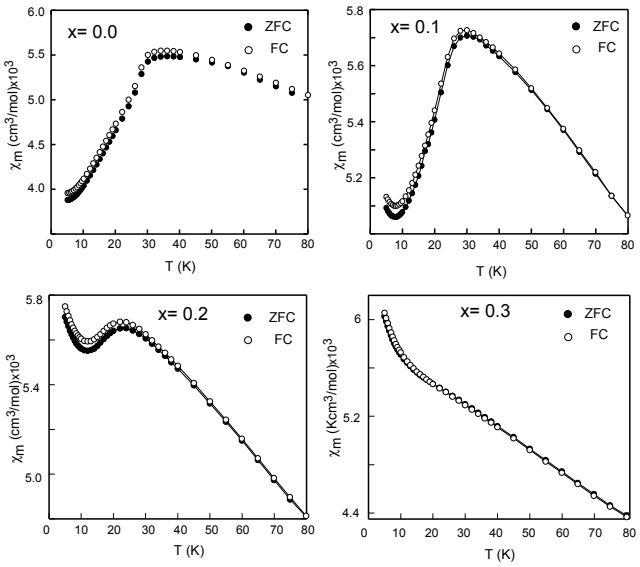

Fig. 6 Magnetic susceptibility measurements in ZFC and FC conditions for the x = 0.0, 0.1, 0.2 and 0.3 compositions.

View Article Online
DOI: 10.1039/C6DT02473D

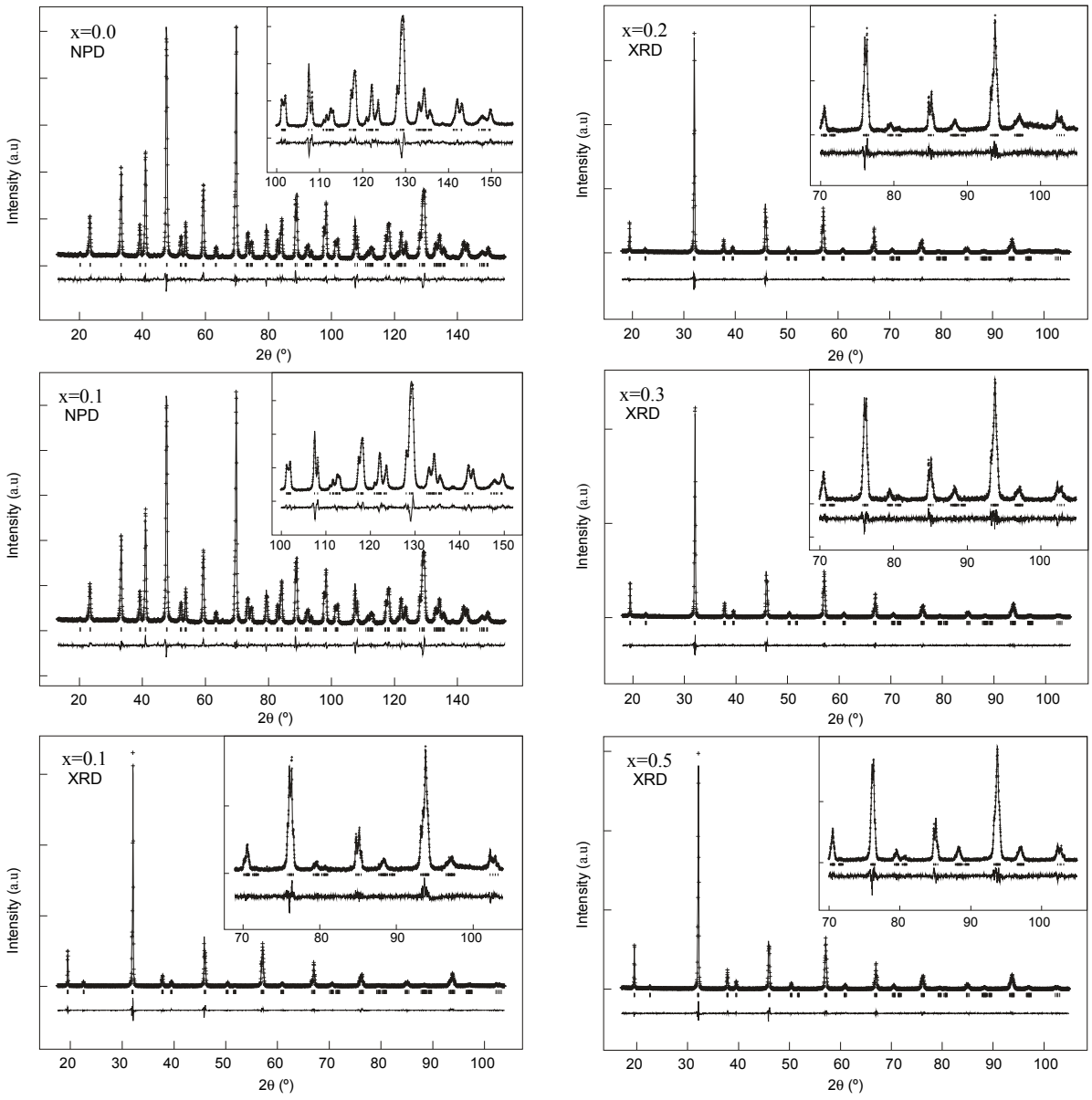

Fig. 7 Experimental (symbols) and calculated (line) X-ray profiles and neutron profiles for the Rietveld refinement of the $Sr_2Ni_{1-x}Mg_xTeO_6$ series at room temperature using a structural model with $I2/m$ space group for (x=0.1, 0.2, 0.3 and 0.5). The bars in the lower part of the graphics represent the Bragg peak positions.

View Article Online
DOI: 10.1039/C6DT02473D

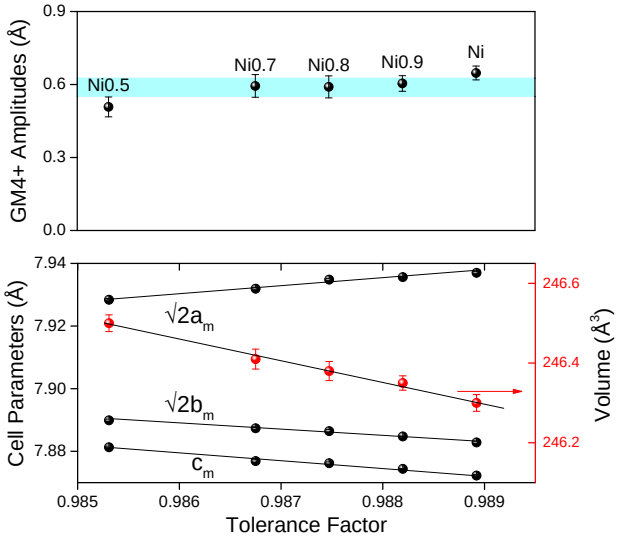

Fig. 8 Variation, as function of the tolerance factor, of (upper) the distortion-amplitude transforming according to the GM_4^+ irrep and (lower) the cell parameters (black) and the unit-cell volume (blue) at room temperature.

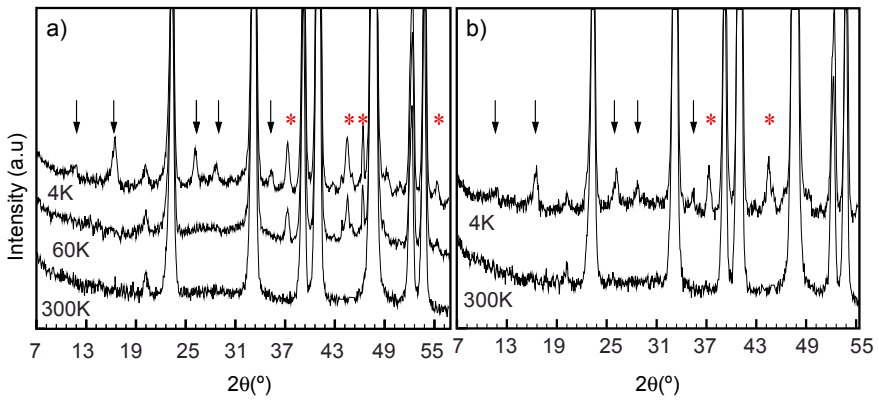

Fig. 9 Diffraction patterns collected on D2B for a) $x = 0.0$ and b) $x = 0.1$ compositions. The arrows point magnetic reflections whereas the stars mark the reflections associated with the $P2_1/n1'$ monoclinic distortion.

View Article Online
DOI: 10.1039/C6DT02473D

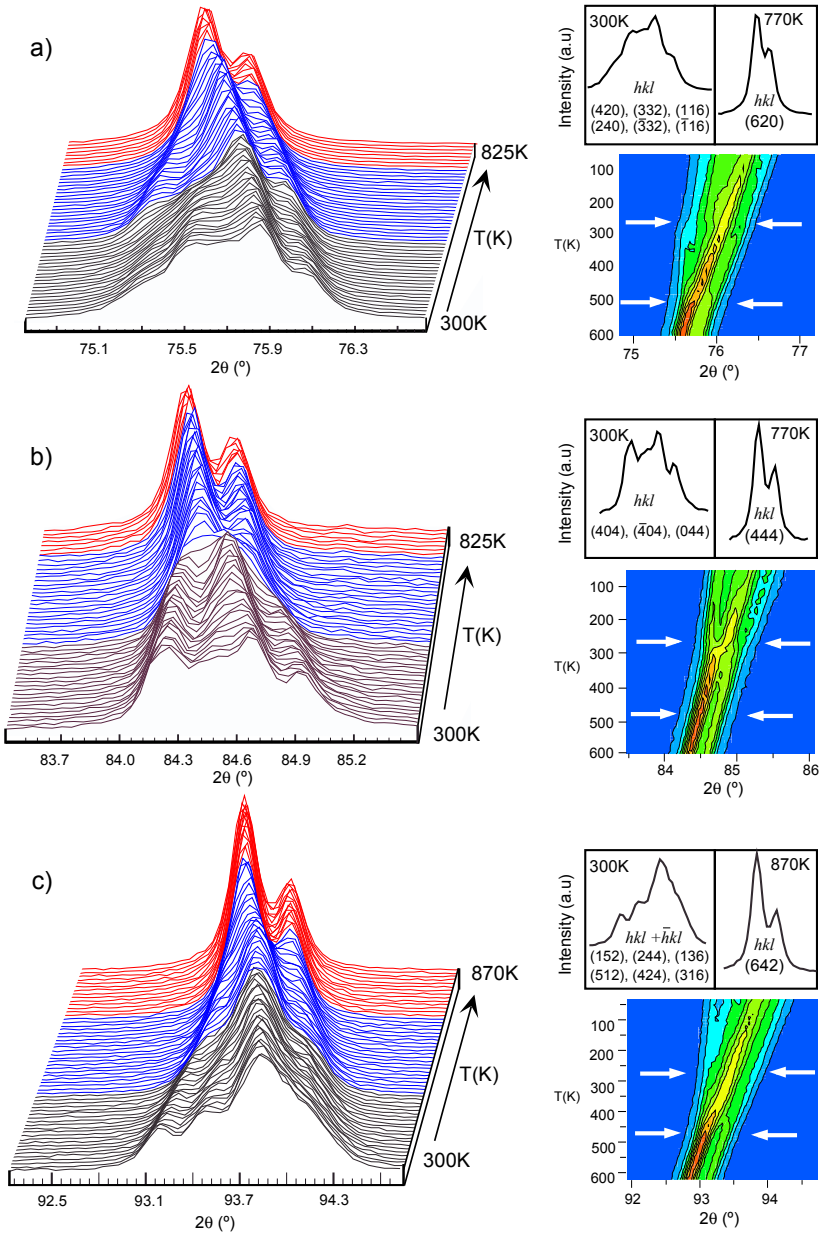

Fig. 10 Thermal evolution of the XRD of Sr_2NiTeO_6 in the intervals: a) $74.8^\circ < 2\theta < 77.3^\circ$, b) $83.3^\circ < 2\theta < 86.2^\circ$ and c) $92^\circ < 2\theta < 95^\circ$ between 300 and 820 K, which correspond to the cubic reflections (620), (444) and (642), respectively.

View Article Online
DOI: 10.1039/C6DT02473D

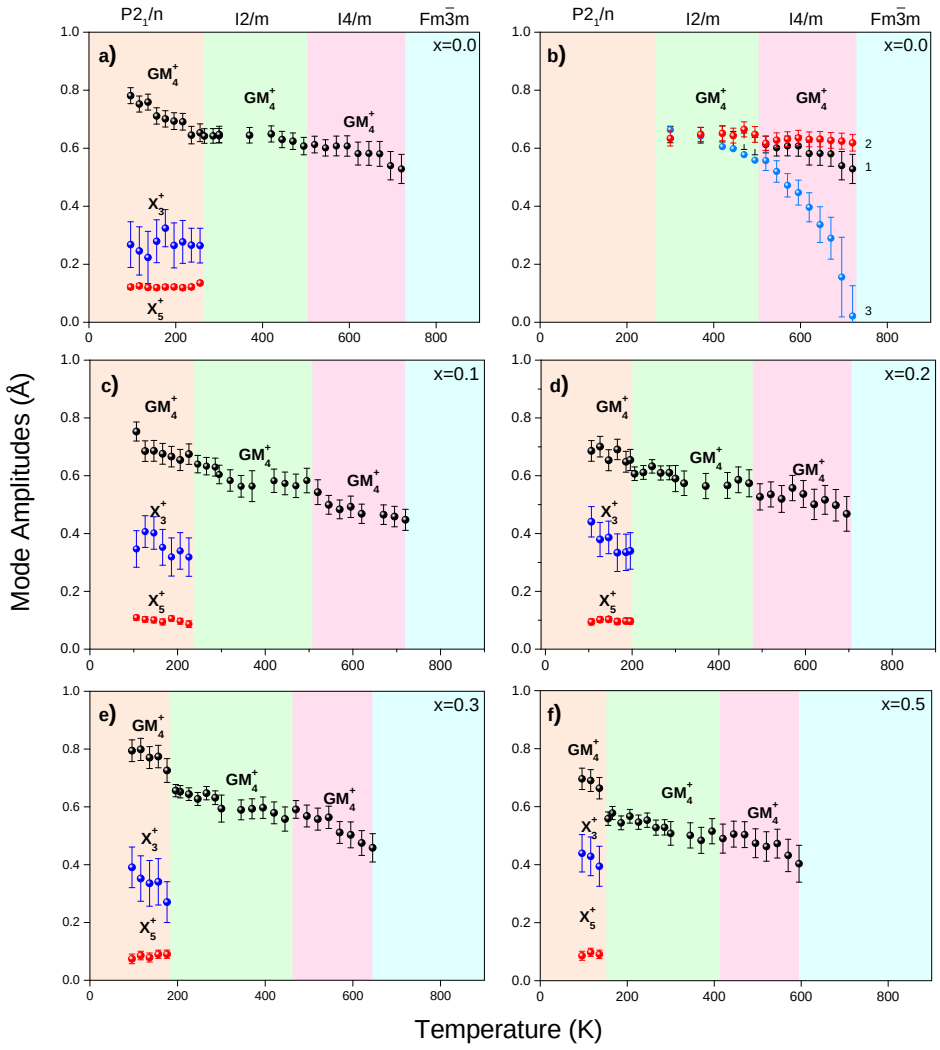

Fig. 11 Temperature dependence of the mode-amplitudes refined in the $P2_1/n$, $I2/m$ and $I4/m$ space groups for the $Sr_2Ni_{1-x}Mg_xTeO_6$ series (x = 0.0, 0.1, 0.2, 0.3 and 0.5)

View Article Online
DOI: 10.1039/C6DT02473D

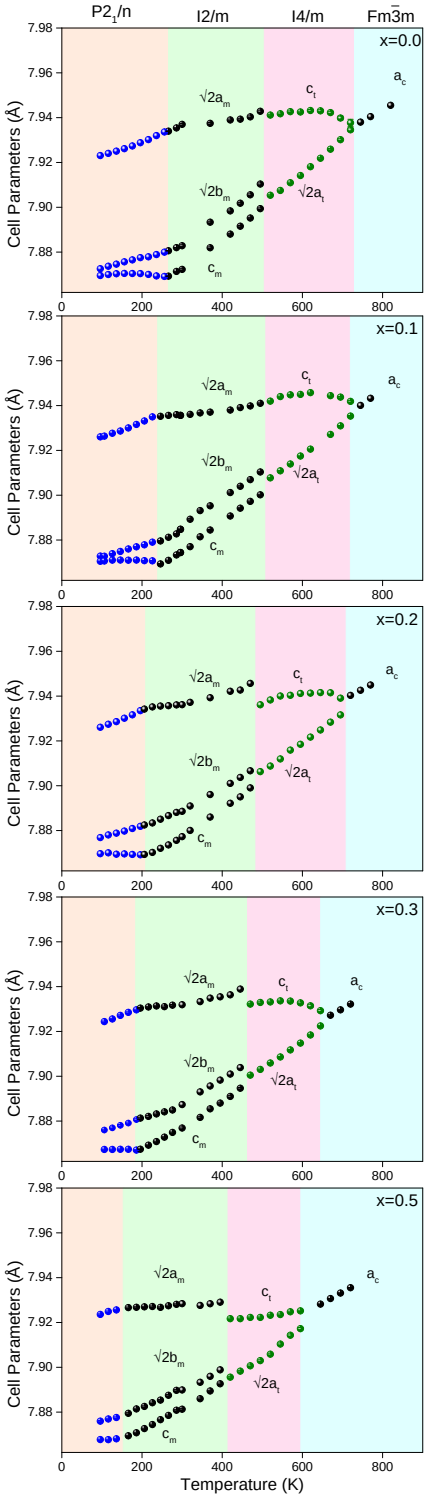

Fig. 12 Thermal evolution of the cell parameters refined in the $P2_1/n$, $I2/m$ and $I4/m$ space groups for the $Sr_2Ni_{1-x}Mg_xTeO_6$ series (x = 0.0, 0.1, 0.2, 0.3 and 0.5)

View Article Online
DOI: 10.1039/C6DT02473D

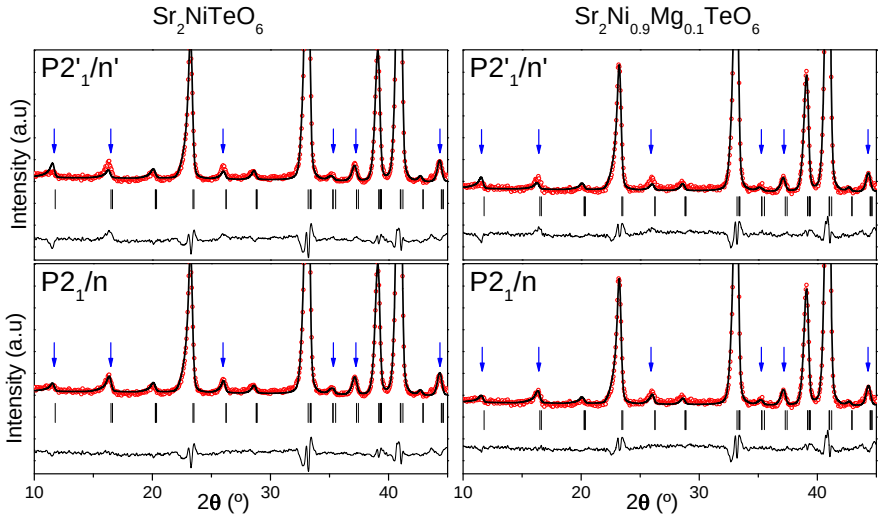

Fig. 13 Refinement results from the neutron diffraction data of the magnetically ordered Sr_2NiTeO_6 and $Sr_2Ni_{0.9}Mg_{0.1}TeO_6$, using both $P2_1/n$ and $P2_1'/n'$ space group models.

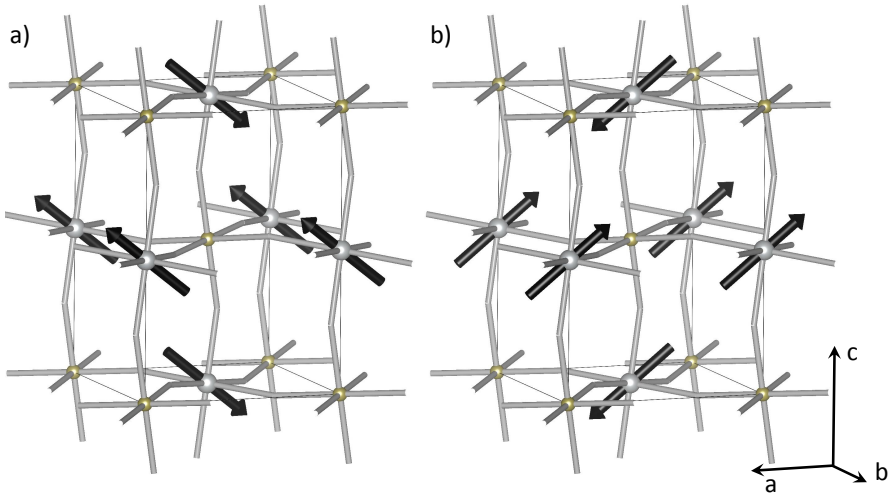

Fig. 14 Sketch of a) Model 1 and b) Model 2 for the magnetic structure of Sr_2NiTeO_6 and $Sr_2Ni_{0.9}Mg_{0.1}TeO_6$ at 4 K.

View Article Online
DOI: 10.1039/C6DT02473D

Table 1 Experimentally observed band sets and the Dq and B parameters for the $Sr_2Ni_{1-x}Mg_xTeO_6$ (x = 0.0, 0.1, 0.2, 0.3 and 0.5) series.

x	0.0	0.1	0.2	0.3	0.5
$\nu_1(cm^{-1})$	6900	6900	6900	6900	6900
$\nu_2(cm^{-1})$	11500	11500	11500	11600	11500
$\nu_3(cm^{-1})$	21600	21600	21650	21650	21650
$\nu_4(cm^{-1})$	13700	13700	13700	13700	13700
$\nu_5(cm^{-1})$	19250	19250	19300	19300	19300
$Dq(cm^{-1})$	690	690	690	690	690
$B(cm^{-1})$	830	830	830	835	840
C (cm^{-1})	3830	3830	3830	3815	3800
ν_1; $^3A_{2g}(^3F) \rightarrow ^3T_{2g}(^3F)$; 10 Dq					
ν_2; $^3A_{2g}(^3F) \rightarrow ^3T_{1g}(^3F)$; $15Dq+7.5B-0.5\sqrt{225B^2+100Dq^2-180DqB}$					
ν_3; $^3A_{2g}(^3F) \rightarrow ^3T_{1g}(^3P)$; $15Dq+7.5B+0.5\sqrt{225B^2+100Dq^2-180DqB}$					
ν_4; $^3A_{2g}(^3F) \rightarrow ^1E_g(^1D)$; $8B+2C-(6B^2/10Dq)$					

Table 2 Magnetic parameters for $Sr_2Ni_{1-x}Mg_xTeO_6$, (0.0, 0.1, 0.2, and 0.3) oxides obtained by dc-susceptibility (^{dc}) and neutron-diffraction (nd) measurements. J_1 and J_2 have been calculated from the following equations taken from Blassse Blasse[24]: $k_B\theta_A$ = 2/3 S(S + 1)(12J_1 + 6J_2) and k_BT_N=-2/3 S(S + 1)(6J_2) where T_N= Néel temperature, θ_A the Weiss temperature and S= the total spin of the paramagnetic ions.

x	0.0	0.1	0.2	0.3
T_N^{dc} (K)	35	29	23	17
T_N^{nd} (K)	35	29	–	–
θ^{dc} (K)	–225	–204	–196	–144
$\frac{J_1}{J_2}$	2.7	3.0	3.7	3.7
C_m^{dc} (cm^3 K/mol)	1.55	1.45	1.31	0.99
μ_{eff}^{dc} (μ_B)	3.52	3.40	3.23	2.81
M_{Ni}, 4K	1.78	1.8	–	–

View Article Online
DOI: 10.1039/C6DT02473D

Table 3 Crystal structural data and refinement results for $Sr_2Ni_{1-x}Mg_xTeO_6$ (x = 0.0, 0.1, 0.2, 0.3 and 0.5), at room-temperature. The refinements have been done freeing only one mode-amplitude (see text): GM_4^+, the primary mode for the transition from the cubic $Fm\bar{3}m$ to the monoclinic $I2/m$.

		Sr_2NiTeO_6	$Sr_2Ni_{0.9}Mg_{0.1}TeO_6$	$Sr_2Ni_{0.8}Mg_{0.2}TeO_6$	$Sr_2Ni_{0.7}Mg_{0.3}TeO_6$	$Sr_2Ni_{0.5}Mg_{0.5}TeO_6$
GM_4^+		0.6473(4)	0.6043(1)	0.5902(2)	0.5940(6)	0.5078(1)
Sr	x	0.00000	0.00000	0.00000	0.00000	0.00000
	y	1/2	1/2	1/2	1/2	1/2
	z	-0.75000	-0.75000	-0.75000	-0.75000	-0.75000
	$B_{iso}(^2)$	0.58(3)	0.50(3)	0.94(2)	0.57(3)	0.51(3)
O1	x	0.24714	0.24714	0.24714	0.24714	0.24714
	y	0.24714	0.24714	0.24714	0.24714	0.24714
	z	-0.0272(1)	-0.0239(1)	-0.023(2)	-0.023(1)	-0.0227(18)
	$B_{iso}(^2)$	0.95(1)	1.06(1)	1.27(1)	1.00(1)	1.28(4)
O2	x	0.054(3)	0.048(3)	0.046(4)	0.046(4)	0.045(4)
	y	0	0	0.00000	0	0
	z	-0.75286	-0.75286	-0.7528	-0.75286	-0.75286
	$B_{iso}(^2)$	0.95(1)	1.06(1)	1.27(1)	1.00(1)	1.28(4)
Te	$B_{iso}(^2)$	0.61(1)	0.51(1)	0.49(1)	0.56(1)	0.62(1)
Ni/Mg	$B_{iso}(^2)$	0.61(1)	0.51(1)	0.49(1)	0.56(1)	0.62(1)
Order(%)		100	100	93	92	92
a (Å)		5.6123(2)	5.6113(1)	5.6108(3)	5.6087(3)	5.6062(3)
b (Å)		5.5740(3)	5.5754(1)	5.5766(4)	5.5772(4)	5.5790(3)
c (Å)		7.8722(4)	7.8744(1)	7.8762(4)	7.8768(4)	7.8812(4)
β (°)		246.27(2)	246.35(1)	246.44(2)	246.41(6)	246.50(2)
V (Å^3)		89.965(4)	89.967(4)	89.967(1)	89.966(5)	89.965(5)
R_p(%)		8.02	8.74	9.2	9.12	9.01
R_{wp}(%)		6.2	7.5	8.1	8.41	8.37
R_{exp}(%)		5.61	6.03	5.88	5.81	5.71
χ^2		10.7	10.8	11.13	11.48	11.05
R_{Bragg}		5.61	5.54	7.07	6.84	6.77

View Article Online
DOI: 10.1039/C6DT02473D

Table 4 Main bond distances (Å), selected angles (°), and Φ(Φ′) and Ψ(Ψ′) tilt angles, for $Sr_2Ni_{1-x}Mg_xTeO_6$ (x=0.0, 0.1, 0.2, 0.3 and 0.5) at room temperature. The values were obtained refining the mode breaking the symmetry from the cubic $Fm\bar{3}m$ to the monoclinic $I2/m$.

	Sr_2NiTeO_6	$Sr_2Ni_{0.9}Mg_{0.1}TeO_6$	$Sr_2Ni_{0.8}Mg_{0.2}TeO_6$	$Sr_2Ni_{0.7}Mg_{0.3}TeO_6$	$Sr_2Ni_{0.5}Mg_{0.5}TeO_6$
Ni/MgO_6 octahedra					
Ni/Mg-O1	2.011(1)×4	2.010(1)×4	2.009(1)×4	2.008(1)×4	2.007(1)×4
Ni/Mg-O2	2.012(2)×2	2.009(1)×2	2.008(2)×2	2.009(2)×2	2.008(2)×2
Average distance	2.011(6)	2.010(6)	2.009(6)	2.008(6)	2.007(1)
Predicted distance	2.040	2.043	2.046	2.049	2.055
TeO_6 octahedra					
Te-O1	1.966(1)×4	1.964(1)×4	1.964(1)×4	1.963(1)×4	1.962(1)×4
Te-O2	1.968(2)×2	1.965(1)×2	1.965(2)×2	1.964(2)×2	1.963(2)×2
Average distance	1.967(6)	1.964(6)	1.964(1)	1.964(6)	1.962(6)
Predicted distance	1.910	1.910	1.915	1.916	1.917
∠O1-Ni/Mg-O2	89.9(2)	89.8(2)	89.9(2)	90.1(1)	90.1(2)
∠O2-Ni/Mg-O2	89.1(1)	89.0(7)	90.0(7)	90.1(7)	90.2(7)
∠O1-Te-O2	89.8(4)	89.9(4)	89.9(4)	89.9(4)	89.9(4)
∠O2-Te-O2	89.1(4)	90.1(4)	90.1(4)	90.1(4)	90.1(4)
∠Ni/Mg-O1-Te	164.5(1)	164.7(5)	164.5(1)	163.7(2)	163.5(2)
∠Ni/Mg-O2-Te	169.1(1)	169.0(8)	169.1(2)	168.6(3)	168.2(4)
$\Phi(TeO_6)/\Phi'(Ni/MgO_6)$	8.852(2)	7.879(1)	7.551(2)	7.547(2)	7.345(2)
$\Psi(TeO_6)/\Psi'(Ni/MgO_6)$	8.656(2)	7.704(1)	7.385(2)	7.379(2)	7.181(2)

View Article Online
DOI: 10.1039/C6DT02473D

Table 5 Crystal structural data for $Sr_2Ni_{1-x}Mg_xTeO_6$ (x = 0.0, and 0.1), at 4K. The refinements have been done freeing only their mode-amplitude (see text): GM_4^+, X_3^+ and X_5^+ the primary modes for the transition from the cubic $Fm\bar{3}m$ to the monoclinic $P2_1/n$.

		Sr_2NiTeO_6	$Sr_2Ni_{0.9}Mg_{0.1}TeO_6$
Sr	x	0.0000	0.0000
	y	0.4959(11)	0.4930(8)
	z	0.2500	0.2500
	$B_{iso}(^2)$	0.78(2)	0.77(2)
O1	x	-0.7718(3)	-0.7656(3)
	y	0.2560(3)	0.2599(3)
	z	-0.0249(1)	-0.0254(1)
	$B_{iso}(^2)$	1.08(2)	1.23(2)
O2	x	-0.4501(2)	-0.4492(2)
	y	0.5000	0.50000
	z	-0.2579(2)	-0.2528(1)
	$B_{iso}(^2)$	1.08(2)	1.23(2)
O3	x	-0.2560(3)	-0.2599(3)
	y	0.2282(3)	0.2344(3)
	z	0.0249(1)	0.0254(1)
	$B_{iso}(^2)$	1.08(2)	1.23(2)
Te	$B_{iso}(^2)$	0.83(2)	0.89(2)
Ni/Mg	$B_{iso}(^2)$	0.83(2)	0.89(2)
a (Å)		5.6046(2)	5.6052(1)
b (Å)		5.5649(3)	5.5667(1)
c (Å)		7.8707(4)	7.8718(1)
β (°)		245.48(2)	245.62(1)
V (Å^3)		89.958(4)	89.955(4)
R_p(%)		4.90	5.54
R_{wp}(%)		6.48	7.12
R_{exp}(%)		4.46	4.01
χ^2		3.7	3.15
R_{Bragg}		4.85	4.44

Table 6 Refined parameters of the magnetic structures of Sr_2NiTeO_6 and $Sr_2Ni_{0.9}Mg_{0.1}TeO_6$ at 4 K. Only the spin components of Ni atoms in $(0,0,\frac{1}{2})$ are given. The data can not distinguish Model 1 from Model 2.

Ni at $(0,0,\frac{1}{2})$	Sr_2NiTeO_6	$Sr_2Ni_{0.9}Mg_{0.1}TeO_6$
Model 1		
M_x	1.18(7)μ_B	1.23(8)μ_B
M_y	0	0
M_z	1.34(6)μ_B	1.34(7)μ_B
$\mathbf{M_{Ni}}$	1.78(9)μ_B	1.8(1)μ_B
δ	42(3)°	43(3)°
Model 2		
M_x	−1.18(7)μ_B	−1.23(8)μ_B
M_y	0	0
M_z	1.34(6)μ_B	1.34(7)μ_B
$\mathbf{M_{Ni}}$	1.78(9)μ_B	1.8(1)μ_B
δ	−42(3)°	−43(3)°

Table 7 Observed low temperature magnetic moments in several Ni^{2+} containing ordered perovskites obtained above and below the Néel temperature, T_N, from magnetic susceptibility and neutron data, respectively.

Perovskite	T_N (K)	θ(K)	J_1/J_2	M_{eff} (μ_B) T≫T_N	M_{Ni} (μ_B) 4K*	Ref.
Sr_2NiMoO_6	81	–	–	–	1.92	35
Ba_2NiMoO_6	64	–	–	–	2.04	35
Ba_2NiWO_6	48	–120	0.8	3.02	1.9(3)	36,37
$SrLaNiSbO_6$	26	–	–	2.83	1.53(5)	38
La_2NiTiO_6	25	–	–	3.12	2.05(4)	39
Sr_2NiTeO_6	35	–240	3.0	3.06	–	6
	35	–225	2.7	3.52	1.78(9)	This work
$Sr_2Ni_{0.9}Mg_{0.1}TeO_6$	29	–204	3.0	3.40	1.8(1)	This work

* From NPD data.

View Article Online
DOI: 10.1039/C6DT02473D

References

1 G. R. Rossman, R. D. Shannon and R. K. Waring, *Journal of Solid State Chemistry*, 1981, **39**, 277 – 287.

2 W. D. J. Evans, *Trans. British Cer. Soc.*, 1968, **67**, 397–419.

3 Y. N. Venevtsev, E. D. Politova and G. S. Zhdanov, *Ferroelectrics*, 1974, **8**, 489–490.

4 E. D. Politova and Y. N. Venevtsev, *Dokl. Akad. Nauk SSSR*, 1973, **209**, 838–841.

5 P. Köhl, E. Schultze-Rhonhof and D. Reinen, *Zeitschrift fÃijr anorganische und allgemeine Chemie*, 1970, **378**, 129–143.

6 D. Iwanaga, Y. Inaguma and M. Itoh, *Materials Research Bulletin*, 2000, **35**, 449 – 457.

7 C. J. Howard, B. J. Kennedy and P. M. Woodward, *Acta Crystallographica Section B*, 2003, **59**, 463–471.

8 L. Ortega-San Martín, J. P. Chapman, G. Cuello, J. González-Calbet, M. I. Arriortua and T. Rojo, *Zeitschrift für anorganische und allgemeine Chemie*, 2005, **631**, 2127–2130.

9 R. Ubic, S. Letourneau, S. Thomas, G. Subodh and M. T. Sebastian, *Chemistry of Materials*, 2010, **22**, 4572–4578.

10 R. Ubic, S. Letourneau and S. Thomas, *J. Aus. Ceram. Soc*, 2011, **47**, 49.

11 L. Ortega-San Martín, J. P. Chapman, L. Lezama, J. Sanchez-Marcos, J. Rodriguez-Fernandez, M. I. Arriortua and T. Rojo, *J. Mater. Chem.*, 2005, **15**, 183–193.

12 L. Ortega-San Martín, J. P. Chapman, E. Hernández-Bocanegra, M. Insausti, M. I. Arriortua and T. Rojo, *Journal of Physics: Condensed Matter*, 2004, **16**, 3879–3888.

13 B. Orayech, L. Ortega-San-Martin, I. Urcelay-Olabarria, L. Lezama, T. Rojo, M. I. Arriortua and J. M. Igartua, *Dalton Trans.*, 2015, **44**, 13716–13734.

14 B. Orayech, A. Faik, G. A. López, O. Fabelo and J. M. Igartua, *Journal of Applied Crystallography*, 2015, **48**, 318–333.

15 B. Orayech, I. Urcelay-Olabarria, G. A. Lopez, O. Fabelo, A. Faik and J. M. Igartua, *Dalton Trans.*, 2015, **44**, 13867–13880.

16 B. Orayech, A. Faik and J. Igartua, *Polyhedron*, 2016, **Accepted**, Effect of the M^{3+} cation size on the structural and high temperature phase transitions in Sr_2MSbO_6 (M = Ln, Y) double perovskites.

17 H. M. Rietveld, *J. Appl. Cryst.*, 1969, **2**, 65.

18 V. Petricek, M. Dusek and L. Palatinus, *Z. Kristallogr.*, 2004, **229**, 345–352.

19 K. Momma and F. Izumi, *Journal of Applied Crystallography*, 2008, **41**, 653–658.

20 P. Atkins, T. Overton, J. Rourke, M. Weller, F. Armstrong, P. Salvador, M. Hagerman, T. Spiro and E. Stiefel, *Shriver and Atkins Inorganic Chemistry (4th ed.)*, New York: W.H. Freeman and Company, 2006, pp. 478–483.

21 B. E. Douglas, D. McDaniel and J. Alexander, *Concepts and models of inorganic chemistry*, 3rd ed. John Wiley and Sons: New York, 1994.

22 A. Abragam and B. Bleaney, *Electron Paramagnetic Resonance of Transition Ions*, Dover Publications: New York, 1986.

23 F. E. Mabbs and D. J. Machin, *Magnetism and transition metal complexes*, Chapman and Hall: Londres, 1973.

24 G. Blasse, *Philips Res. Repts.*, 1965, **20**, 327–336.

25 P. Battle, J. Goodenough and R. Price, *Journal of Solid State Chemistry*, 1983, **46**, 234 – 244.

26 P. Battle and W. Macklin, *Journal of Solid State Chemistry*, 1984, **54**, 245 – 250.

27 P. Battle and W. Macklin, *Journal of Solid State Chemistry*, 1984, **52**, 138 – 145.

28 E. Iturbe-Zabalo, J. M. Igartua, A. Larrañaga, V. Pomjakushin, G. R. Castro and G. J. Cuello, *Journal of Physics: Condensed Matter*, 2013, **25**, 205401.

29 A. Zaraq, B. Orayech, A. Faik, J. Igartua, A. Jouanneaux and A. E. Bouari, *Polyhedron*, 2016, **110**, 119 – 124.

30 E. Iturbe-Zabalo, A. Faik, A. Larrañaga, M. Hoelzel, G. Cuello and J. M. Igartua, *J. Solid State Chem.*, 2013, **198**, 24–38.

31 D. Orobengoa, C. Capillas, M. I. Aroyo and J. M. Perez-Mato, *J. Appl. Cryst.*, 2009, **A42**, 820–833.

32 T. K.-Y. Wong, B. J. Kennedy, C. J. Howard, B. A. Hunter and T. Vogt, *Journal of Solid State Chemistry*, 2001, **156**, 255 – 263.

33 S. Vasala, J.-G. Cheng, H. Yamauchi, J. B. Goodenough and M. Karppinen, *J. Chem. Mater*, 2012, **24**, 2764–2774.

34 M. Cecilia Blanco, S. Alexis Paz, V. M. Nassif, J. J. Guimpel and R. E. Carbonio, *Dalton Trans.*, 2015, **44**, 10860.

35 M. Martínez-Lope, J. Alonso, M. Casais and M. Fernández-Díaz, *European Journal of Inorganic Chemistry*, 2002, **2002**, 2463–2469.

36 Y. Todate, *Journal of Physics and Chemistry of Solids*, 1999, **60**, 1173 – 1175.

37 D. E. Cox, G. Shirane and B. C. Frazer, *Journal of Applied Physics*, 1967, **38**, 1459–1460.

38 M. Attfield, P. Battle, S. Bollen, T. Gibb and R. Whitehead, *Journal of Solid State Chemistry*, 1992, **100**, 37 – 48.

39 E. Rodriguez, M. L. Lopez, J. Campo, M. L. Veiga and C. Pico, *J. Mater. Chem.*, 2002, **12**, 2798–2802.